BCM3D 2.0: Accurate segmentation of single bacterial cells in dense biofilms using computationally generated intermediate image representations

Ji Zhang[1,§], Yibo Wang[1,§], Eric Donarski[1], Andreas Gahlmann[1,2,*]

[1]Department of Chemistry, University of Virginia, Charlottesville, Virginia, USA

[2]Department of Molecular Physiology & Biological Physics, University of Virginia School of Medicine, Charlottesville, Virginia, USA

§These authors contribute equally to this paper

*Corresponding Author: agahlmann@virginia.edu

Abstract

Accurate detection and segmentation of single cells in three-dimensional (3D) fluorescence time-lapse images is essential for observing individual cell behaviors in large bacterial communities called biofilms. Recent progress in machine-learning-based image analysis is providing this capability with every increasing accuracy. Leveraging the capabilities of deep convolutional neural networks (CNNs), we recently developed bacterial cell morphometry in 3D (*BCM3D*), an integrated image analysis pipeline that combines deep learning with conventional image analysis to detect and segment single biofilm-dwelling cells in 3D fluorescence images. While the first release of *BCM3D* (*BCM3D 1.0*) achieved state-of-the-art 3D bacterial cell segmentation accuracies, low signal-to-background ratios (SBRs) and images of very dense biofilms remained challenging. Here, we present *BCM3D 2.0* to address this challenge. *BCM3D 2.0* is entirely complementary to the approach utilized in *BCM3D 1.0*. Instead of training CNNs to perform voxel classification, we trained CNNs to translate 3D fluorescence images into intermediate 3D image representations that are, when combined appropriately, more amenable to conventional mathematical image processing than a single experimental image. Using this approach, improved segmentation results are obtained even for very low SBRs and/or high cell density biofilm images. The improved cell segmentation accuracies in turn enable improved accuracies of tracking individual cells through 3D space and time. This capability opens the door to investigating time-dependent phenomena in bacterial biofilms at the cellular level.

42 **Introduction**

43 Most terrestrial bacteria live in extended 3-dimensional tissue-like communities, named
44 biofilms. As multicellular communities, bacteria can successfully colonize various biotic and
45 abiotic surfaces. Biofilm-dwelling bacteria interact intimately not only with each other and the
46 surface they reside on, but also with a self-produced extracellular matrix (ECM) that consists of
47 proteins, DNA, and polysaccharides[1-3]. The sum total of these interactions helps biofilms develop
48 emergent capabilities beyond those of isolated cells[1, 2, 4, 5]. Most notably, biofilms are more tolerant
49 towards physical, chemical, and biological stressors[5-7]. Understanding how such capabilities
50 emerge from the cooperative or antagonistic behaviors among individual cells requires live-cell
51 compatible imaging technologies that are capable of resolving and tracking single cells within
52 dense 3D biofilms.

53 Recently developed light sheet-based fluorescence imaging modalities combine high
54 resolution with fast imaging speed and low phototoxicity at levels that cannot be matched by
55 confocal microscopy[8-10]. Light sheet-based microscopy modalities are therefore increasingly used
56 for non-invasive time-lapse imaging of eukaryotic cells and tissues[11-13] as well as bacterial
57 biofilms[14-16]. Depending on the type of biofilm, the cell density may however be too high to clearly
58 resolve the gaps between cells with diffraction-limited microscopy. Super-resolution imaging
59 modalities, such as structured illumination microscopy[17, 18], improve the spatial resolution, but
60 experimental improvements in spatial resolution always come at the cost of decreased temporal
61 resolution and increased light exposure to the specimen, which again raises photobleaching and
62 phototoxicity concerns[19, 20]. An additional challenge arises for cell tracking studies. Tracking
63 motile cells may require high frame rate imaging to achieve sufficient temporal resolution. Higher
64 frame rates need to be accompanied by a proportional decrease in excitation laser intensities to

65 mitigate photobleaching and phototoxicity. The decreased excitation laser intensities then result in
66 lower signal-to-background ratios (SBRs) in the individual images. The inherent trade-offs
67 between spatial and temporal resolution, SBR, and photobleaching and phototoxicity is driving the
68 continued development of new and improved image processing approaches that extract ever
69 increasing amounts of useful information from the available experimental images.

70 Image processing pipelines based on supervised training of deep convolutional neural
71 networks (CNNs) have been shown to outperform conventional image processing approaches for
72 a variety of tasks in biomedical image analysis[21, 22]. For 3D biofilm image segmentation, we have
73 recently developed Bacterial Cell Morphometry 3D (*BCM3D 1.0*), which achieved state-of-the-
74 art performance for bacterial cell counting and cell shape estimation[23]. *BCM3D 1.0* does not rely
75 on manually annotated training data, but instead combines *in silico*-trained CNNs for voxel
76 classification with graph-theoretical linear clustering (mLCuts[24]) to post-process the thresholded
77 CNNs outputs (i.e. the confidence maps for voxel-level classification). Using this approach,
78 *BCM3D 1.0* automatically identifies individual cells in 3D images of 3D bacterial biofilms, reports
79 their 3D shape and orientation, and classifies cell types with different morphologies. However,
80 processing images with low SBRs and high cell densities remains challenging. Specifically, over-
81 and under-segmentation errors increase in frequency for low SBR and high cell density images.

82 *Cellpose*[25] ,*StarDist*[26] and the work by Scherr *et al.*,[27] are CNN-based approaches that
83 create intermediate image representations for better segmentation. We reasoned that solving an
84 image-to-image translation task may prove to be a more robust strategy for handling extreme
85 imaging conditions than the voxel classification approach implemented in *BCM3D 1.0* or, at least,
86 yield complementary segmentation results to *BCM3D 1.0*. Two different intermediate image
87 representations are generally employed. The first representation is used to locate objects and the

88 second representation is used to highlight the boundaries of objects. In previous work[25-27], the
89 CNN-predicted Euclidean distance to the nearest background pixel/voxel or the CNN-predicted
90 object/background probability map was used to locate objects. Generation of boundary
91 representations vary more widely: *StarDist* and *Cellpose* use star-convex polygons and spatial
92 gradients separately to give complete boundaries, which can be used for object shape estimation.
93 Scherr *et al*. instead enhance boundary regions that are close to other objects to prevent them from
94 merging. Inspired by these approaches, we expanded the *BCM3D* workflow with a complementary
95 CNN-based processing pipeline that translates the raw 3D fluorescence images into two distinct
96 intermediate image representations that, in combination, are more amenable to conventional
97 mathematical image processing, namely seeded watershed[28] and Otsu thresholding[29]. For object
98 localization, we adapted the approach used by *StarDist*[26] and Scherr et al.[27]. For boundary
99 information, however, we generated a new intermediate image representation that provides a
100 complete 3D boundary of an object and additionally highlights whether the boundary is near other
101 objects. We establish that, when combined and processed appropriately, these intermediate image
102 representations provide biofilm segmentation results with higher accuracy than *BCM3D 1.0*.
103 Importantly and in contrast to *BCM3D 1.0*, generation of intermediate image representations does
104 not require image deconvolution as a pre-processing step. Deconvolution can lead to noise
105 amplification[30] that then leads to false positive segmentation objects with physiologically
106 unreasonable shapes. We show that, using intermediate image representations, experimentally
107 acquired biofilm images can be successfully segmented using CNNs trained with computationally
108 simulated biofilm images – a feature that provides the flexibility to segment a wide variety of
109 different cell shapes. Finally, we show that improvements in segmentation accuracy enables

110 accurate multi-cell tracking, which is demonstrated using 3D simulated and experimental time-
111 lapse biofilm images.
112
113 **Methods**
114 **Lattice Light Sheet Microscope Imaging of Bacterial Biofilms**
115 Fluorescence images of bacterial biofilms were acquired on a home-built lattice light sheet
116 microscope (LLSM). LLSM enables specimen illumination with a thin light sheet derived from a
117 2D optical lattice[31, 32]; here, an intensity uniform light sheet was produced by dithering a square
118 lattice. The average illumination intensity across the light sheet was less than 1 W/cm^2. The sub-
119 micrometer thickness of the light sheet is maintained over a propagation distance of ~30 μm to
120 achieve high resolution, high contrast imaging of 3D specimens comparable to confocal
121 microscopy but with lower concomitant photobleaching and phototoxicity. Widefield fluorescence
122 images of illuminated planes in the specimen are recorded on a sCMOS detector (Hamamatsu
123 ORCA Flash v2). 3D biofilm images were acquired by translating the specimen through the light
124 sheet in 200 nm step sizes using a piezo nano-positioning stage (Mad City Labs, NanoOP100HS).
125 The data acquisition program is written in LabVIEW 2013 (National Instruments).
126 Kanamycin resistant *S. oneidensis* MR-1, constitutively expressing GFP, were cultured at
127 30 °C overnight in LB medium with 50 μg/ml Kanamycin. Overnight cultures were diluted 100
128 times into the same culture medium, grown to an optical density at 600 nm (OD600) of 0.4 – 1.0,
129 and then diluted to OD600 ~ 0.05 using M9 media with 0.05% (W/V) casamino acids. Poly-l-
130 lysine coated round glass coverslips with the diameter of 5 mm were put into a 24-well plate
131 (Falcon) and 400 μL of diluted cell culture was added to the well. Cells were allowed to settle to
132 the bottom of the well and adhere to the coverslip for 1 hour. After the settling period, the coverslip

133 was gently rinsed with M9 media to flush away unattached cells. Then 400 μL of M9 media (0.05%
134 casamino acids) were added to ensure immersion of the coverslips. The well plate was set in a
135 30 °C chamber for 72-96 hours to allow dense biofilms to develop. Media were exchanged every
136 24 hours. Before imaging, the coverslip was rinsed again with fresh M9 media. The rinsed
137 coverslip was then mounted onto a sample holder and placed into the LLSM sample-basin filled
138 with M9 media. GFP was excited using 488 nm light sheet excitation. 3D biofilm stacks were
139 acquired by translating the specimen through the light sheet in 200 nm or 235 nm steps. Each 2D
140 slice was acquired with an exposure time of 5 ms or 10 ms.

141 Samples for time-lapse images were prepared by the same procedures, except imaging was
142 started after either 24-hour or 48-hour cell attachment period, and the imaging experiment was
143 carried out in LM medium (0.02% (W/V) yeast extract, 0.01% (W/V) peptone, 10 mM HEPES
144 (pH 7.4), 10 mM $NaHCO_3$) with a lactate concentration of 0.5 mM.[33] Time-lapse images were
145 recorded every 30 seconds for 15 minutes or 5 minutes for 5 hours for the two datasets shown in
146 **Figure 5** with the same imaging parameters as detailed above.

147

148 **Raw Data Processing**

149 Raw 3D stacks were deskewed and rotated as described previously[34], but the deconvolution
150 step was omitted. If necessary, background subtraction can be applied to reduce background signal.
151 3D images were rendered using the 3D Viewer plugin in Fiji[35] or ChimeraX[36]. Sample drift over
152 the course of a time-lapse imaging experiment was corrected by Correct 3D Drift[37], a Fiji plug-in
153 that performs registration by phase correlation, a computationally efficient method to determine
154 translational shifts between images at two different time points.

155

156 **Generation of simulated biofilm images**

157 Data for CNNs training was computationally generated as described previously[23]. Briefly,
158 CellModeller[38], an individual-based computational model of biofilm growth, was used to simulate
159 growth and division of individual rod-shaped cells in a population (**Figure 1a**). A minimum
160 distance criterion between cells is imposed at each time point to alleviate cellular collisions that
161 are due to cell growth. We chose cell diameter and cell length (d, l) parameters consistent with a
162 given bacterial species, namely (1 μm, 3 μm) for *E. coli*[39], (0.7 μm, 6 μm) for *M. xanthus*[40], and
163 (0.6 μm, 2 μm) for *S. oneidensis*[41]. 3D fluorescence intensity images (**Figure 1b**) were generated
164 by convolving randomly positioned fluorophores in the cytoplasm or the membranes of simulated
165 cells (**Figure 1cd**) with experimentally measured point spread functions (PSFs), and then adding
166 experimentally measured background and noise (Poisson detection noise, based on the summed
167 background and signal intensities, as well as Gaussian read noise, experimentally calibrated for
168 our detector at 3.04 photons per pixel on average)[42].

169 The fluorescence signal intensity in the simulated images was adjusted to match the signal
170 to background ratios (SBRs) of experimentally acquired data. To estimate the SBRs of both
171 simulated and experimental images, we manually selected 10 'signal' and 10 'background' regions
172 in the images. The SBR was calculated by dividing the mean background intensity by the mean
173 signal intensity. To estimate the local density of a biofilm, the image was partitioned into several
174 3D tiles 64 by 64 by 8 voxels in size and the total cell volume contained in each tile was divided
175 by the tile volume. The reported cell density was computed as the average of the 10 densest tiles
176 for each dataset.

177

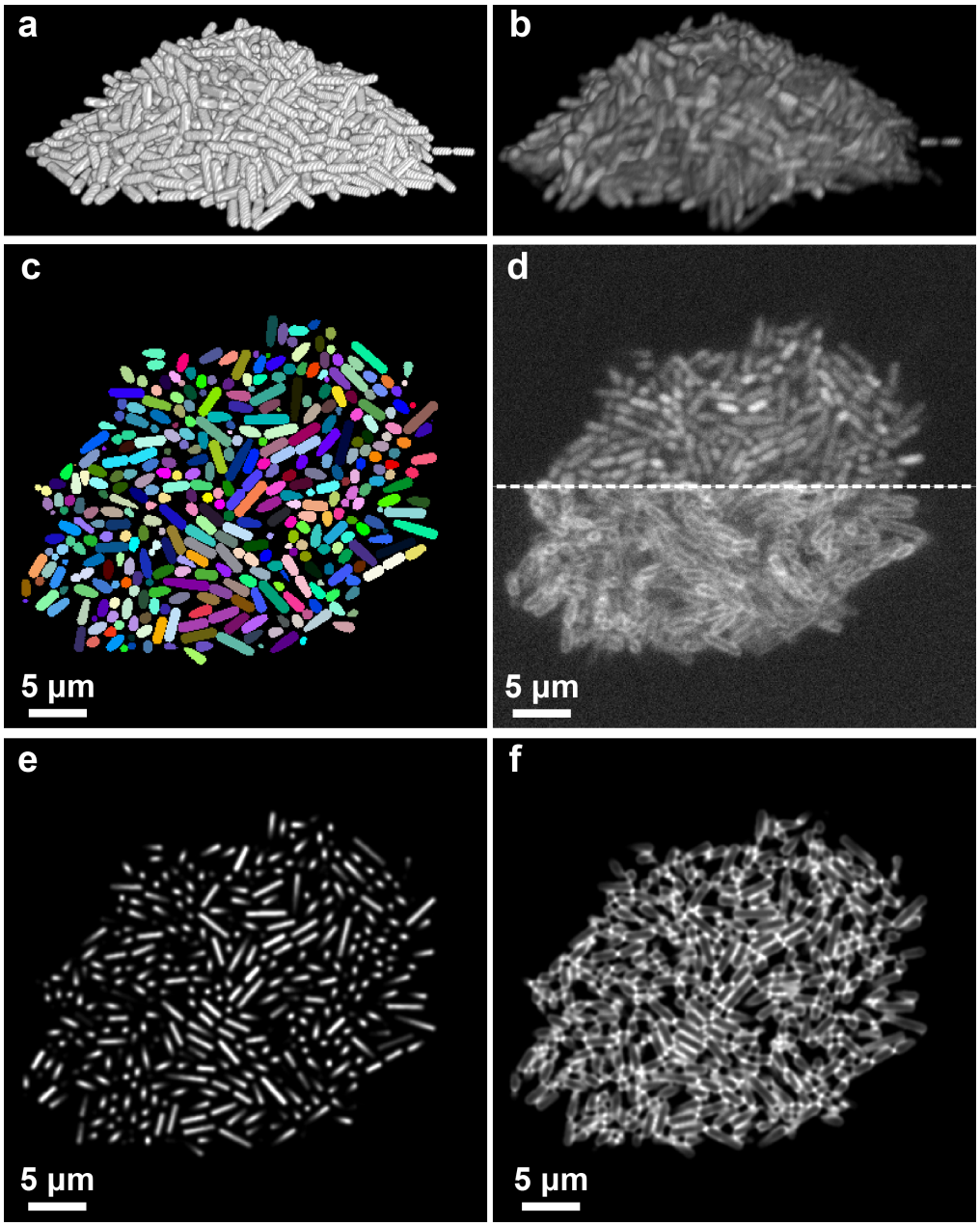

Figure 1. Simulation of fluorescent biofilms images and intermediate image representations. (a) Cell arrangements obtained by CellModeller. (b) Simulated 3D fluorescence image based on the cell arrangements in a. (c) Ground truth information of a 2D slice. Different cells are shown in different colors and intercellular spaces (background voxels) are displayed in black. (d) 2D slices of the simulated fluorescence image corresponding to the ground truth shown in c. The upper panel shows cells containing cytosolic fluorophores, the lower panel shows cells with fluorescently stained membranes. (e and f) Intermediate image representations generated from the ground truth information shown in c. See text for details.

Generation of intermediate image representations

To generate 'distance to nearest cell exterior' images (**Figure 1e**, **Figure S1**) from ground truth data, the Euclidean distance of each voxel inside a cell to the nearest voxel not belonging to that cell was calculated. The so-obtained distances were then normalized to the maximum value of that cell (**Figure S1c**). In order to obtain a steeper gradient in distance values, the distance values were additionally raised to the third power (**Figure S1d**), so that the resulting images show highly peaked intensity near the cell center. In a final step, the 'distance to nearest cell exterior' images were smoothed by Gaussian blurring (kernel size = 5 voxels in each dimension) (**Figure S1e**).

To help distinguish touching cells, we calculated a second image representation, the 'proximity enhanced cell boundary' image (**Figure 1f**, **Figure S1**). First, we subtracted the normalized distances to the nearest voxel not belonging to this cell (**Figure S1c**) from the binary map (**Figure S1f**). Second, we calculated the inverse of the Euclidean distance of each voxel inside a cell to the nearest voxel belonging to another cell, an intermediate image representation that has been proven useful to prevent objects merging in 2D[27] (**Figure S1g**). These two intermediate images were then multiplied together (**Figure S1h**) and small holes in the resulting images (**Figure S1h inset**) were filled using grayscale closing (**Figure S1i inset**). The resulting intermediate images provides a complete boundary of an object but also highlights whether the boundary is in close proximity to any other objects. Compared to previous methods that only provide a complete boundary or only provide boundary areas that are close to any other objects, this new intermediate image representation provides a more informative boundary representation. In a final step, the 'proximity enhanced cell boundary' images were smoothed by Gaussian blurring (kernel size = 5 voxels in each dimension) (**Figure S1i**). Post-processing of these intermediate image representations by, single- and multilevel Otsu thresholding[29, 43], and seeded watershed[28] from the

210 scikit-image Python library[44] (**see SI**) produced visually accurate segmentation results (**Figure S2,**
211 **S3**).
212
213 **Training the convolutional neural network**
214 To generate the above-mentioned intermediate image representations from experimental
215 data, we trained 3D U-Net Based CNNs using the CSBDeep Python package[19]. We employed a
216 network architecture depth of 2, a convolution kernel size of 3, 32 initial feature maps, and a linear
217 activation function in the last layer. To achieve robust performance, we trained this network using
218 ten to twenty simulated biofilm images with randomly selected cell densities and signal-to-
219 background ratio. To ensure the broad applicability of these networks, half of these images were
220 biofilms containing cells expressing cytosolic fluorescence and the other half were biofilms
221 containing membrane-stained cells (see **Figure 1d**). Instead of directly learning the intermediate
222 image representations g(x) from the input raw data x, the networks were trained to learn the
223 residual $\tilde{g}(x)$ to the input of the networks, i.e. $g(x) = \tilde{g}(x) + x$. This strategy provides better
224 performance, because solvers are more efficient in solving residual functions than unreferenced
225 functions[45]. The loss function was taken as the mean absolute error (MAE) between the generated
226 and the target images. The networks were trained for 100 epochs with 100 parameter update steps
227 per epoch and an initial learning rate 0.0004. The learning rate is reduced by a half if the validation
228 loss is not decreasing over 10 epochs. Using these parameters, it took approximately 1 hour to train
229 the CNNs on a NVIDIA Tesla V100 GPU with 32 GB memory.
230 To test whether segmentation objects have physiologically reasonable cell shapes, we
231 trained a 3D CNNs based classification model using tensorflow 2.0. We adapted a network
232 architecture from Zunair et.al.,[46]; mainly includes three 3D convolutional layers, one global
233 average pooling layer and a sigmoid activation function in the last layer. To achieve robust

performance, we trained this network using 733 manually confirmed segmentation objects from experimental data (411 reasonable shaped objects, 322 oddly shaped objects). Training data were augmented by rotation and flip. The loss function was taken as the binary cross entropy between the model output and the corresponding target value. The networks were trained for 100 epochs with a batch size of 5 and an initial learning rate 0.0002. The learning rate is reduced by a half if the validation loss is not decreasing over 15 epochs. Using these parameters, it took approximately 17 mins to train the CNNs on a NVIDIA Tesla V100 GPU with 32 GB memory.

Tracking

Simpletracker in MATLAB was used to build tracking graphs and spatially resolved lineage trees[47]. *Simpletracker* implements the Hungarian algorithm and nearest neighbor trackers for particle tracking that links particles between frames in 2D or 3D. We used 1 μm and 1.5 μm as the maximum distance threshold for cell linking for simulated and experimental data, respectively. We used the nearest neighbor algorithm to associate the centroids of segmented objects in subsequent frames, such that the closer pairs of centroids are linked first. In order to determine a cell division event, a distance threshold of 1 μm and 1.5 μm for simulated and experimental data, respectively, a cell volume threshold of 1.5 (parent cell should be 1.5 times larger than the daughter cell), and a cell length threshold of 1.5 (parent cell should be 1.5 times longer than the daughter cell), were used to determine parent-daughter relationships between cell pairs on consecutive frames.

Performance evaluation

Segmentation accuracy was quantified as cell counting accuracy and cell shape estimation accuracy. The cell counting accuracy (CA) was calculated as previously described[23]:

$$CA = \frac{TP}{TP + FP + FN}$$

where, TP is the number of truth positive objects, FP is the number of false positive objects, and FN is the number of false positive objects. Cell shape estimation is evaluated by two separate measures. Single-cell segmentation accuracy (SSA) takes the mean Intersection-over-Union (IoU) value (aka the Jaccard index[48]) over segments that have a matching ground truth/manual annotation object:

$$SSA = \frac{1}{N_{match}} \sum_{i}^{N_{match}} \frac{|Seg_i \cap GT_i|}{|Seg_i \cup GT_i|}$$

where, $|Seg_i \cap GT_i|$ is volume of overlap between the predicted object and the ground truth object, and $|Seg_i \cup GT_i|$ is the volume enclosed by both the predicted object and the ground-truth object. We note that the SSA metric can take on high values even if the shape of a segmented object does not accurately represent the shape of the corresponding ground truth object. For example, a predicted round object with a diameter of 20 covered by a ground truth square object with a length of 20 gives a 0.8 IoU value, which could be interpreted as good performance. From a biological perspective however, this would signify a substantial inaccuracy in shape estimation. To measure differences in cell shape in a more discriminating way, we additionally computed a single-cell boundary F1 score (SBF1)[49]. The SBF1 of the abovementioned square vs circular object example is 0.67. The SBF1 score is computed as

$$SBF1 = \frac{1}{N_{match}} \sum_{i}^{N_{match}} \frac{2 \cdot prcecision_i \cdot recall_i}{prcecision_i + recall_i}$$

where precision is the ratio of matching boundary points in a matched segmentation object to the total points of its boundary. Similarly, recall is the ratio of the matching boundary points to the total points of ground truth boundary. According to the definition of boundary F1 score[50], a distance error tolerance is used to decide whether a point on the predicted boundary has a match on the ground truth boundary. For our 3D data, we use $\sqrt{3}$ voxels.

To quantify tracking accuracy, we used the acyclic oriented graph metric (*AOGM*)[51]. The *AOGM* value is calculated as the weighted sum of the number of graph operations required to convert the estimated graph to the ground truth graph, i.e.:

$$AOGM = w_{NS}NS + w_{FN}FN + w_{FP}FP + w_{ED}ED + w_{EA}EA + w_{EC}EC$$

The tracking accuracy can then be computed using a normalized *AOGM* value, where $AOGM_0$ is the number of operations to build the ground truth graph from an empty graph:

$$TRA = 1 - min(AOGM, AOGM_0)/AOGM_0$$

There are three types of graph operations that are associated with detection errors: the number of false negatives (*FN*), the number of false positives (*FP*), and the number of missed splits (*NS*: *m* reference cells ($m > 1$) are assigned to a single segmented cell); and three types of graph operations that are associated with object linking: edge deletion (ED), addition (*EA*), and alteration of the semantics of an edge (*EC*: The semantics of an edge can either represent the same cells over time or represent a parent-daughter relationship). To focus on object matching over time (i.e. the association performance of the algorithm), we used an equally weighted sum of the lowest number of graph operations on edges only (*TRA_edge*). To give a more comprehensive view, we used an equally weighted sum of the number of graph operations on all six operations (*TRA_full*).

To estimate tracking accuracy for experimental data, we manually traced a small subset (n = 25) ancestor cells over time based on *BCM3D 2.0* segmentation masks. Two researchers

299 performed tracking independently, manually determining parent-daughter relationships within the
300 lineages originating from the ancestor cells. This lineage information was then used to compute
301 *TRA_edge.*
302
303 **Results**
304 **Cell segmentation using intermediate image representations**
305 High cell density and low SBR datasets are encountered often in biofilm research,
306 especially when cells touch each other and biofilms extend farther into the vertical (*z*-) dimension,
307 so that light scattering becomes pronounced[52]. We therefore sought to specifically improve
308 bacterial cell segmentation accuracy for high cell density and low SBR biofilm images. Our
309 previous approach (*BCM3D 1.0*) relied on deconvolution as a preprocessing step to increase the
310 SBR and to sharpen the image. However, deconvolution can introduce artifacts into an image, such
311 as ringing[53], and noise amplification[54], and thereby introduce errors into the segmentation results.
312 The segmentation pipeline of *BCM3D 2.0*, in contrast, works on the raw image data directly
313 without the need for deconvolution.
314 We compared two commonly used cell labeling approaches, namely cell interior labeling
315 through expression of cytosolic fluorescent proteins and cell membrane staining through
316 membrane-embedded fluorescent dyes. For cell interior labeling (**Figure 2ab**), *BCM3D 2.0*
317 consistently produces cell counting accuracies of >95% for SBRs > 1.3 and cell densities < 65%.
318 A clear drop-off in cell counting accuracy is observed for SBRs of 1.19 but cell counting accuracies
319 of >70% are still achieved even for high cell densities of 65%. The performance of *BCM3D 2.0*
320 on low SBR datasets represents a substantial improvement (>20%) over the performance of
321 *BCM3D 1.0*. Membrane staining (**Figure 2cd**) produces even more challenging images for

322 segmentation, due to the less pronounced fluorescence intensity minima between cells (red arrow
323 in **Figure 2bd**). We again observe a drop in cell counting accuracy for SBRs of 1.19. This drop-
324 off is however much less pronounced than for the previous results obtained with *BCM3D 1.0*, and
325 represents an even larger (>29%) improvement over *BCM3D 1.0* for such extremely low SBR
326 datasets. Visual inspection of slices through the image volumes (**Figure 2bd**) reveals that even for
327 SBR = 1.3, the cell bodies are difficult to distinguish for expert human annotators, especially for
328 membrane-stained cells. Despite the low contrast in the SBR = 1.3 datasets, *BCM3D 2.0* is still
329 able to achieve >90% cell counting accuracies, which, depending on cell density, represents a 6-
330 26% increase over the performance of *BCM3D 1.0*.

331 To determine the improvement in cell shape estimation, we evaluated the cell counting
332 accuracies as a function of IoU matching threshold (the IoU matching threshold is a quantitative
333 measure of cell shape similarity relative to the ground truth) for a SBR of 1.3 and a cell density of
334 62% (**Figure 2ef**). The cell counting accuracies obtained by *BCM3D 2.0* are consistently higher
335 than *BCM3D 1.0* for IoU matching thresholds larger than 0.5, indicating that cell shapes are more
336 accurately estimated by *BCM3D 2.0*. A similar trend is observed for single-cell segmentation
337 accuracy and single-cell boundary F1 score[49] – two additional metrics for segmentation accuracy
338 (**Table 1**). Taken together, these results establish that more robust cell segmentation can be
339 achieved using the *BCM3D 2*.0 image processing pipeline, which uses CNNs to generate two
340 distinct intermediate image representations for subsequent mathematical processing.

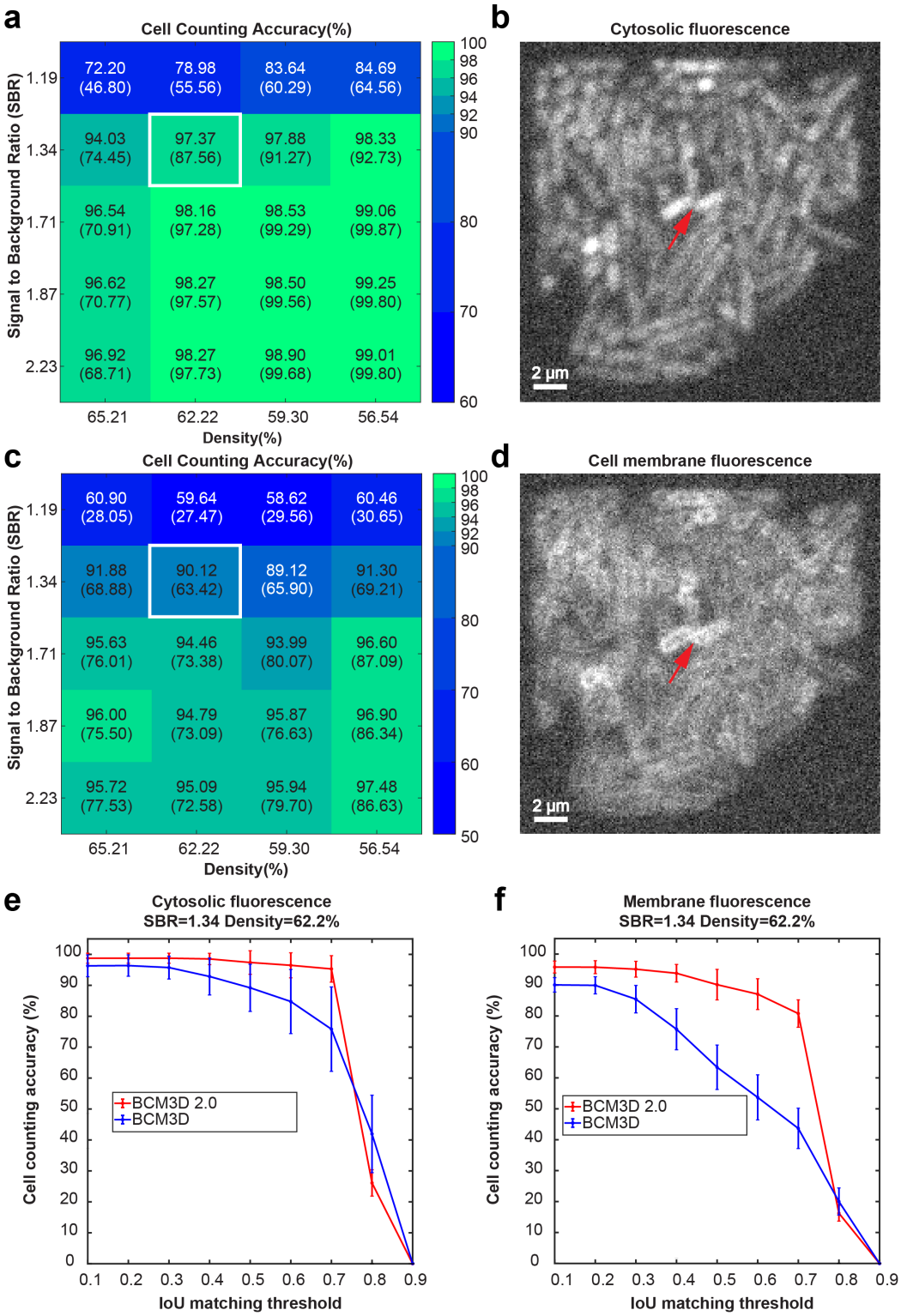

Figure 2. Performance of *BCM3D 2.0* on previously unseen simulated biofilm images. **(a)** Cell counting accuracy (using an IoU matching threshold of 0.5 for each segmented object) averaged over N=10 replicate datasets for cells labeled with cytosolic fluorophores. **(b)** Example image of

cells labeled with cytosolic fluorophores (Cell density = 62.2%, SBR = 1.34, indicated by white rectangle in panel a). **(c)** Cell counting accuracy (using an IoU matching threshold of 0.5 for each segmented object) averaged over *N*=10 replicate datasets for cells labeled with membrane-localized fluorophores. **(d)** Example image of cells labeled with membrane-localized fluorophores (Cell density = 62.2%, SBR = 1.34, indicated by white rectangles in panel c). The red arrow indicates a close cell-to-cell contact. **(e** and **f)** Comparison of segmentation accuracies achieved by *BCM3D 1.0* and *BCM3D 2.0* for cytosolic and membrane labeling, respectively (SBR = 1.34, cell density = 62.2%). Segmentation accuracy is parameterized in terms of cell counting accuracy (*y* axis) and IoU matching threshold (*x* axis). Each data point is the average of *N*=10 independent biofilm images. Data are presented as mean values ± one standard deviation.

Table 1. Quantitative comparison of single cell level segmentation accuracy between *BCM3D 1.0* and *BCM3D 2.0*.

	Cytosolic labeling		Membrane labeling	
	SSA*	SBF1**	SSA*	SBF1**
BCM3D 1.0	0.796 ± 0.021	0.983 ± 0.008	0.756 ± 0.009	0.961 ± 0.007
BCM3D 2.0	0.791 ± 0.004	**0.995** ± **0.001**	**0.773** ± **0.005**	**0.988** ± **0.002**

*SSA and **SBF1 estimate how accurately the shape of a matched object compare with it of the corresponding ground truth. Here, the IoU threshold is 0.5 and the distance error tolerance for SBF1 is $\sqrt{3}$ voxels. (See methods for details). Data are presented as mean values ± one standard deviation, the better performance (if different within error) is marked in bold.

Segmentation of experimentally obtained biofilm images

To test the performance of *BCM3D 2.0* on experimental data, we acquired images of *S. oneidensis* biofilms expressing GFP. Visual inspection of the segmentation results obtained by applying *BCM3D 2.0* (see Methods), showed physiologically reasonable cell shapes for a majority

368 of segmented objects (**Figure 3**). To quantitatively evaluate segmentation performance, manual
369 annotation results are often used as references. However, manual annotation of 3D biofilm images
370 is inconsistent itself and therefore too time consuming to provide reliable results[23], especially for
371 3D data. We therefore chose to assess the segmentation accuracy using representative
372 morphological observables that are available after segmentation, namely object volume, object
373 solidity (volume fraction of the object as compared to the smallest convex polygon that encloses
374 it), major axis length, longer minor axis length, and the ratio of the two minor axes lengths (longer
375 minor axis divided by the shorter one). We performed principal component analysis (PCA) using
376 these morphological observables and project each segmented object onto a plane spanned by the
377 first two principal components. For simulated data (for which the ground truth is known) this
378 approach shows a distribution for which the correctly segmented objects are concentrated near the
379 origin, whereas the incorrectly segmented objects are predominantly located at the periphery
380 (**Figure 3a** inset).

381 We applied the same PCA approach to experimental segmentation results obtained for a
382 *S. oneidensis* biofilm containing ~3000 cells. Similar to simulated data, most of the segmentation
383 objects cluster near the origin of the two principal component axes (**Figure 3a**). However, several
384 segmented objects are asymmetrically scattered around the periphery of the distribution.
385 Inspecting the 3D shapes of a few manually selected objects revealed that, consistent with
386 simulated data, physiologically reasonable cell shapes cluster near the center of the distribution,
387 while oddly shaped objects predominantly localize at the periphery. To automatically separate
388 oddly shaped objects from the physiologically reasonable, rod-shape shaped objects, we trained a
389 3D CNN with manually validated segmentation objects (obtained from experimental data, see
390 methods). The trained network efficiently separates rod-shaped objects (~86% of total) from oddly

shaped objects (~14% of total). This classification enables the display of both subpopulations separately even though they are completely intermixed in 3D space (**Figure 3bc**).

We further compared the distributions of solidity and minor axis ratio between rod-shaped and oddly shaped populations. Rod-shaped objects are characterized high values of solidity and minor axis ratio (**Figure 3de**). In contrast, solidity and minor axis ratio for oddly shaped objects take on values less than one and thus show a much broader distribution (**Figure 3de** insets). These results show that, when using *BCM3D 2.0*, ~86% of cells are segmented with physiologically reasonable cell shapes. The remaining 14% of cells can then be subjected to further processing to identify and correct the remaining segmentation errors[23, 24, 49] and/or be subjected to further scrutiny to determine whether they are due to aberrant cell shapes exhibited by sick or intoxicated cells[55].

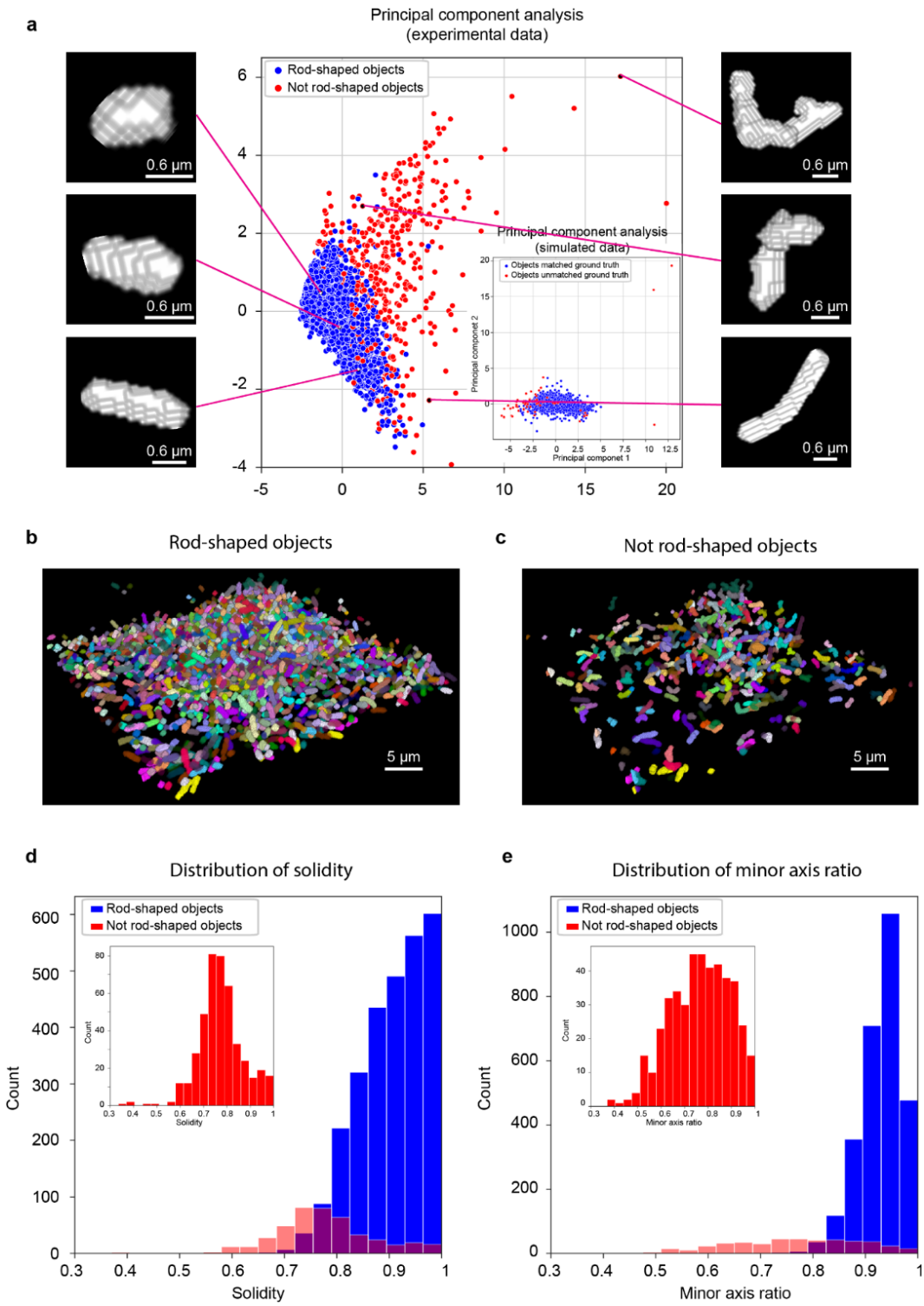

Figure 3. Performance of *BCM3D 2.0* on experimental biofilm images. (a) Principal component analysis of the segmentation objects (obtained from experimentally acquired images) that were classified by a pre-trained 3D CNN as either physiologically reasonable rod-shaped cells or oddly

shaped (not-rod shaped) cells. Three examples cell shapes of each class are shown to the right and left, respectively. Inset: same analysis on simulated biofilm images. (b) 3D segmentation results for objects classified as physiologically reasonable rod-shaped cells. (c) 3D segmentation results for objects classified as oddly shaped. (d) and (e) Comparison of the solidity and minor axis ratio distributions of rod-shaped and oddly shaped objects.

Accurate *BCM3D 2.0* segmentation enables multi-cell tracking in biofilms.

Simultaneous multi-cell tracking and lineage tracing is critical for analyzing single-cell behaviors in bacterial biofilms. We asked whether the cell segmentation performance of *BCM3D 2.0* was sufficient to enable accurate tracking of individual cells in biofilms. To address this question, we employed a tracking-by-detection approached using simulated biofilm images of different SBRs (**Figure 4a**). We evaluated tracking accuracy, as a function of SBR, using the widely used *TRA* metrics based on Acyclic Oriented Graph Matching (AOGM)[51]. In acyclic oriented graphs, cells in different time frame are represented as vertices and linkages between cells from frame-to-frame are represented as edges. When the cells (vertices) are placed at their actual (x,y,z) spatial coordinates, then the cell linkages (edges) represent the branches of a spatially resolved lineage tree (**Figure 4b**). The *TRA* metrics quantify the minimum number of elementary graph operations that are needed to transform an estimated graph into a ground truth graph. *TRA_edge* considers three edge operations only, while *TRA_full* considers all six graph operations[51].

To link the same cells across two different time points, we used a nearest neighbor algorithm[56]. When using spatial distance as the sole metric for cell linking, the AOGM tracking accuracy has a positive correlation with SBR (**Figure 4c**), which highlights the importance of accurate cell segmentation in multi-object tracking-by-detection[57]. *BCM3D 2.0* enables a tracking

accuracy that is similar to the ground truth tracking accuracy (same nearest neighbor tracking algorithm applied to the ground truth segmentation masks) for SBRs of 1.65 and higher. We note that, given the high cell density in this test dataset, the ground truth tracking accuracy does not reach the optimum (100%) even with error-free segmentation. This is due to inherent limitations in how mother daughter relationships are assigned. At SBR's less than 1.65, tracking accuracy decreases rapidly due to the lack of consistent segmentation results. The importance of accurate segmentation is clearly evidenced by the linear dependence of *TRA* as a function of cell counting accuracy (**Figure 4d**).

Another key factor for simultaneous multi-object tracking is the time resolution[57]. The relative movement (RM) of objects from frame to frame is therefore a useful metric to quantify the level of difficulty for cell tracking. The relative movement ($RM_{i,j}$) in time frame i, for a given cell j is defined as the ratio between the distance of cell j to itself between frame i and i+1 and the distance of cell j in frame i to its closest neighbor at frame i + 1. The $<RM>$ metric is then the average $RM_{i,j}$ of all cells for each frame[58]. A dataset with $<RM>$ values of 1 or more means that any tracking method that considers only distance (and distance related features) is likely to fail, whereas a dataset with a $<RM>$ value of less than 0.5 is considered challenging[58]. For the simulated biofilm images here, RM~0.2, which indicates that the time resolution may be good enough for single cell tracking using a nearest neighbor algorithm. Indeed, under these conditions, many cells can be tracked for several generations (**Figure 4b**). However, even at RM~0.2, some cell division events are missed, so that a few branches of the lineage tree are not successfully traced. Even so, the subset of correctly detected cell division events allows for the estimation single-cell doubling cycles in the biofilm (**Figure 4e**). To quantify these trends, we tested how time resolution affects tracking accuracy. When the time resolution is decreased by a factor of two and three, the

455 *TRA_edge* metrics decrease from 91% to 87% and 81%, respectively. The percentage of the parent-
456 daughter misassignment error, quantified as the edge-correction (EC) error over the number of
457 total errors, increases from 1.4% to 3.6 and to 5.2 % (**Figure 4f**). Taken together, these results
458 show that segmentation based multi-object tracking accuracy is highly dependent on segmentation
459 accuracy (which depends on image SBR and cell density[23]) as well as time resolution. It is critical
460 to consider these parameters, when single-cell resolved observables, such as cell trajectories, single
461 cell volume increases, and single-cell doubling times, need to be measured.
462

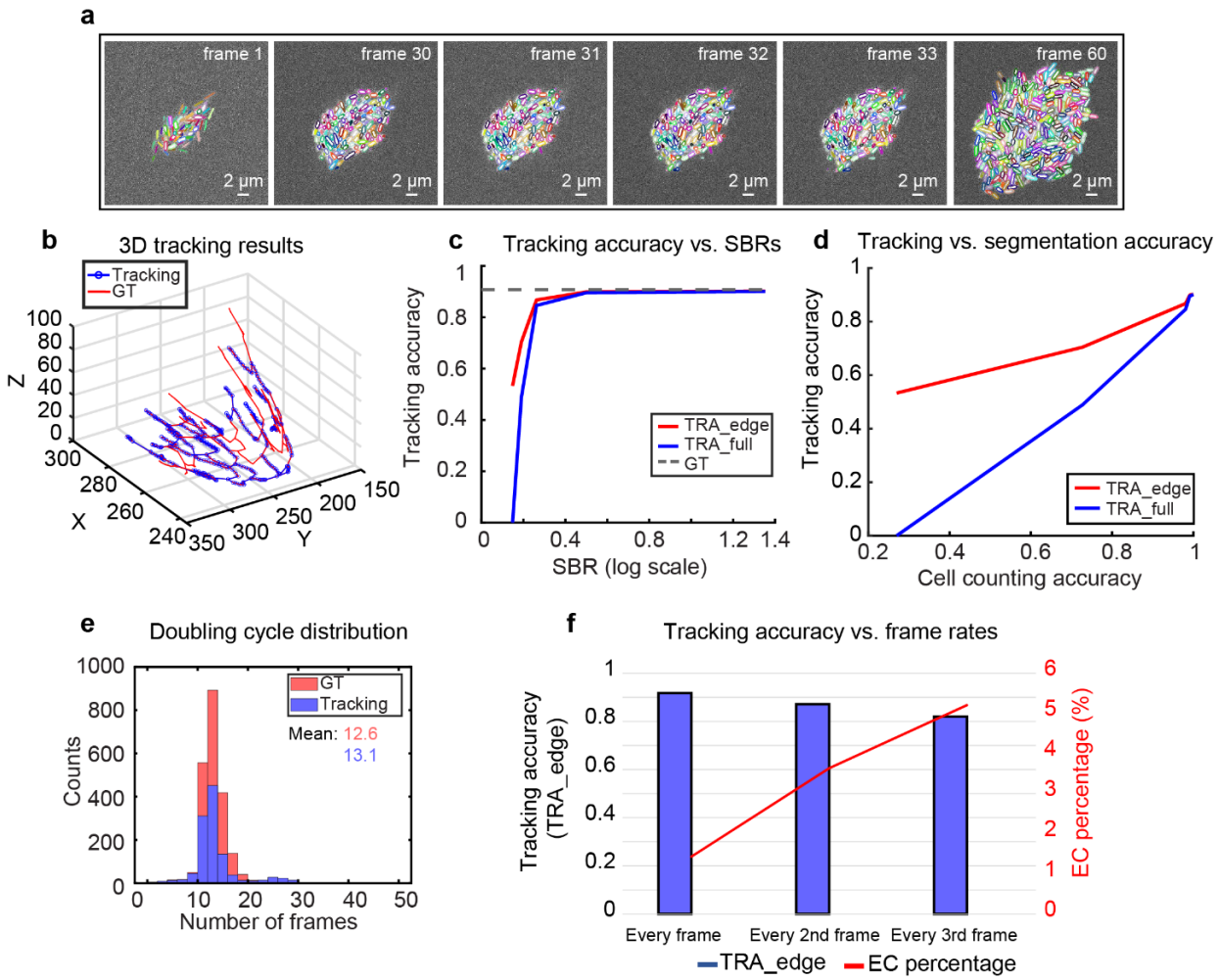

Figure 4. Multi-cell tracking in simulated biofilms. (a) Simulated fluorescence time-lapse images of growing *E. coli*-like biofilm. The SBRs of these images are ~1.65. Contours are color-coded based on segmentation and tracking results. (b) An example of 3D tracking and lineage tracing for simulated biofilm images. For clarity, spatial trajectories and lineages originating from only a single ancestor cell is displayed. The estimated graph is shown in blue and the corresponding ground truth graph is shown in red. The entire biofilm contains over sixty graphs of this type. (c) Two AOGM metrics calculated as *TRA_edge* and *TRA_full* are plotted against image SBR. The grey dashed line indicates tracking of the GT segmentation using the same tracking algorithm. (d) Same data as in panel c plotted as a function of cell counting accuracy at IoU = 0.5, a segmentation accuracy metric that increases for increasing SBR in the raw images[59]. (e) Doubling cycle distribution of simulated data and corresponding tracking results. A completed cell cycle is defined as a track in which the parent cell is able to split twice. This threshold results in a lower count

476 numbers of estimated cell division, but does not alter the shape of the distribution. (f) *TRA_edge*
477 (left axis) and edge correction (EC) percentage (right axis) for different temporal sampling rates.
478 EC percentage indicates how many parent-daughter relationships are misassigned based on the
479 tracking results.
480

481

482 **Multi-cell tracking in the initial phase of *S. oneidensis* biofilm**

483 Cell segmentation and subsequent multi-cell tracking in experimentally acquired 3D
484 images presents additional challenges that were not modeled in the computationally simulated data.
485 These challenges include optical aberrations in the imaging system, broader cell shape
486 distributions in experimental biofilms, cell motility, and association and dissociation dynamics of
487 individual cells to and from the biofilm. To determine whether the *BCM3D 2.0* segmentation
488 results enable improved multi-cell tracking using a nearest neighbor algorithm, we manually traced
489 a subset of ancestor cells over the course of a 15-minute 3D biofilm movie acquired with a time
490 resolution of 30 seconds (**Figure 5ab**). Manual determination of cell-to-cell correspondences in
491 consecutive image volumes generated 583 cell-cell and 3 parent-daughter linkages. Taking this
492 manual annotation as the reference graph, the *RM* metric was determined to be ~0.2 and the
493 *TRA_edge* metric was determined to be 93.5%. Steadily increasing single cell volumes for four
494 selected cells allowed us to measure growth rates of 7.4×10^{-3}, 3.8×10^{-3}, 3.4×10^{-3}, and 0.6×10^{-3}
495 μm^3/min (**Figure 5c**). Cell division events are also readily detected by the algorithm as a sudden
496 decrease in cell volume. In two of the four selected cases, cell division led to the dispersal of the
497 daughter cell. We found a high number of cell dispersion events resulting in the termination of
498 trajectories, most often right after cell division (**Figure 5c**).

Although *BCM3D 2.0* in combination with high-frame rate imaging enables accurate cell tracking, it may not be feasible to maintain high-frame rate volumetric imaging for extended periods of time due to phototoxicity and photobleaching concerns. To further test the limits of nearest neighbor tracking, we tracked *S. oneidensis* biofilm growth for five hours at a time resolution of 5 minutes (**Figure 5de**). We manually traced a subset of founder cells over the course of the experiment, generating 262 cell-cell and 17 parent-daughter linkages. The *RM* metric was determined to be ~0.4 and *TRA_edge* metric was determined to be 80.0% for this manually selected subset. While the nearest neighbor tracking algorithm is capable of making overall accurate cell-cell linkages for a few consecutive frames, automated nearest-neighbor tracking of the same cells for long time periods and correctly detecting all cell-division events is not readily possible (**Figure 5f**). It is, however, possible for human annotators to track individual cells from the segmentation results under such imaging conditions. Single-cell growth rates and single-cell division times can then be readily extracted (**Figure 5f, Figure S4, Movie S1**). The measured growth rates are in excellent agreement with the values obtained with high time resolution imaging (**Figure 5c**). A small number of segmentation errors can be detected by manual tracking, as indicated by the boxes in **Figure 5f**), but these errors don't preclude estimations of single-cell observables. These results indicate that quantitate information about single-cell behaviors is contained even in low time resolution 3D movies of bacterial biofilms. Future work will need to focus on extracting the information as accurately as, but faster than, a human annotator.

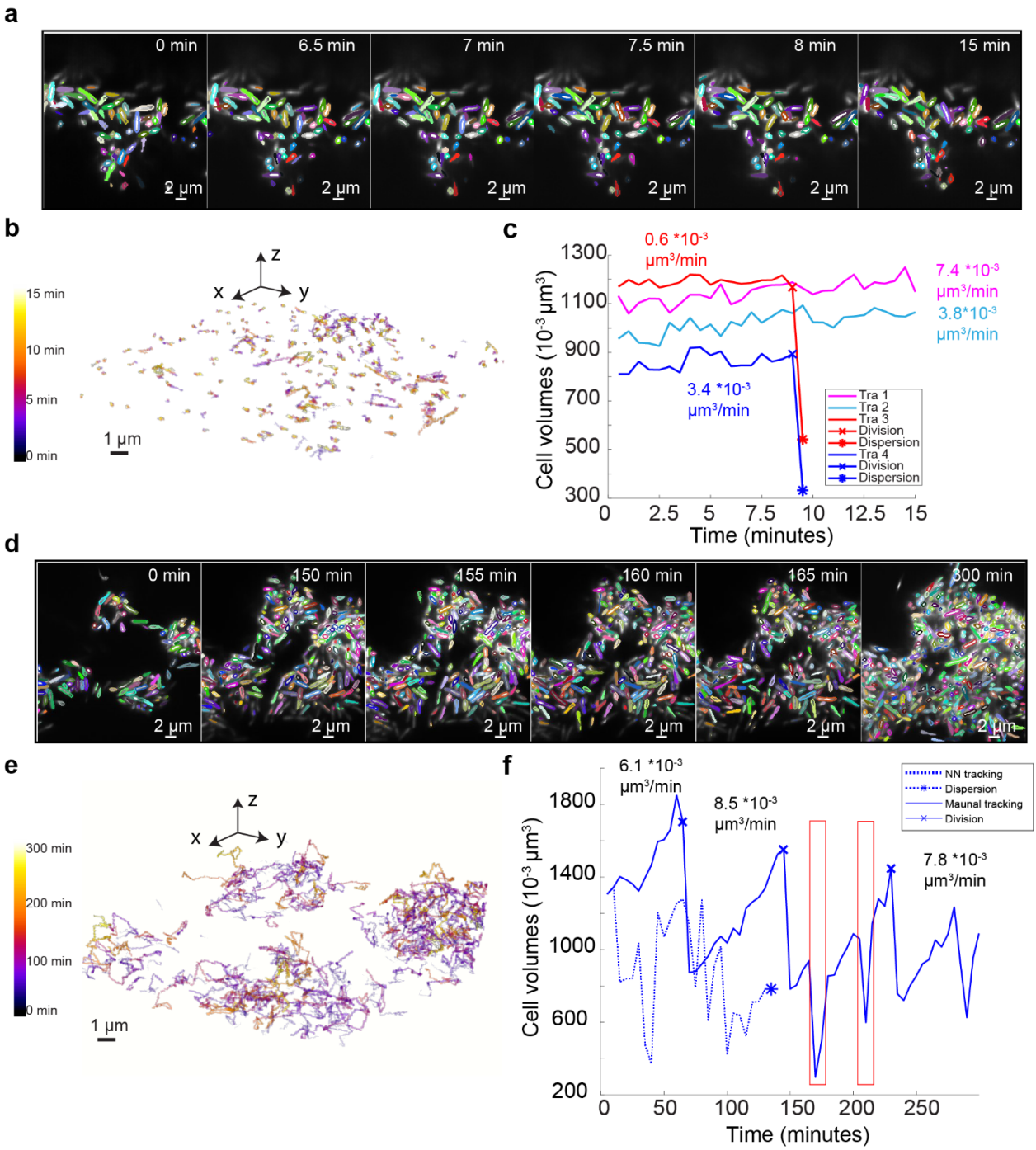

Figure 5. (a) Experimentally acquired fluorescence time-lapse images of a growing *S. oneidensis* biofilm with overlaid single-cell segmentation contours. Images were acquired every 30 seconds for 15 minutes. Corresponding cells in different frames are displayed in the same color. (b) Individual cell trajectories in the biofilm shown in panel a. Cells move very little during the short 15-minute imaging time. (c) Cell volumes over time for four example cells. Cell division and

525 dispersion events are indicated for each trajectory. Single-cell growth rate was measured by
526 calculating the slope of linearly fitted line for each curve (d) Experimentally acquired fluorescence
527 time-lapse images of a growing *S. oneidensis* biofilm with overlaid single-cell segmentation
528 contours. Images were acquired every five minutes for five hours. Corresponding cells in different
529 frames are displayed in the same color. (e) Individual cell trajectories in the biofilm shown in panel
530 a. Cell displacements are more pronounced over the 5-hour imaging time. (f) Evolution of cell
531 volumes over time for a single selected cell. The solid line represents a manually annotated
532 trajectory, and the dashed line represents the nearest neighbor tracking trajectory of the same initial
533 cell. Cell division and dispersion events are indicated on each trajectory. The single-cell growth
534 rate was measured by calculating the slope of the trajectory segment between consecutive cell
535 division events. The red arrow and the boxes indicate periodic underestimation of the cell volume
536 due to oversegmentation.
537

538

539 **Discussion**

540 We expanded the *BCM3D* workflow with a complementary CNN-based processing
541 pipeline, named *BCM3D 2.0*, which transfers raw 3D fluorescence images to intermediate image
542 representations that are more amenable to conventional mathematical image processing
543 (specifically, seeded watershed and single- and multi-level Otsu thresholding). Using the *BCM3D*
544 *2.0* image processing pipeline, improved segmentation results are obtained, especially for
545 challenging datasets characterized by low SBRs and high cell densities. *BCM3D 2.0* consistently
546 achieves better segmentation accuracy than its predecessor, *BCM3D 1.0*, which represented the
547 previous state-of-the-art for 3D cell segmentation in bacterial biofilms.

548 We used the segmentation results provided by *BCM3D 2.0* as the input to a nearest
549 neighbor tracking algorithm to explore the possibility of simultaneous multi-cell tracking in 3D
550 biofilms. We found that accurate multi-cell tracking in 3D time-lapse movies is possible with a

551 nearest neighbor tracking algorithm, only if the relative cell movement (RM) between consecutive
552 frames is small. Depending on the type of biofilm and the bacterial species, small RM values can
553 be achieved using moderate time resolutions of 1-5 minutes. However, for the motile *S. oneidensis*
554 cells imaged here, a time resolution of 5 minutes was insufficient for automated nearest-neighbor
555 cell tracking in dense biofilm regions. Tracking accuracy is reduced especially if cells undergo
556 large and unpredictable displacements within the biofilm, and when cells associate or dissociate
557 to and from the biofilm. Even so, single-cell observables, such as growth rates and cell division
558 times can be extracted based on manual tracking establishing that such information is in fact
559 contained in movies acquired with a time resolution of 5 minutes. Because manual cell tracking is
560 not feasible for biofilms containing thousands of cells, future work will have to focus on extracting
561 this information in an automated manner, efficiently and accurately. Machine-learning based
562 solutions will likely prove to be useful in this context.

563 A clear experimental solution would be to image biofilms at high time resolutions.
564 However, every fluorescence imaging modality is subject to trade-offs between the achievable
565 spatial and temporal resolution, image contrast (SBR), and phototoxicity and photodamage. When
566 imaging *S. oneidensis* biofilms every 30 s, we did not observe any apparent phototoxicity and
567 photodamage to the cells. Even so, after several hours of time-lapse imaging, the majority of cells
568 dispersed from the field-of-view. Whether this behavior is part of a negative phototaxis response
569 of *S. oneidensis* remains to be investigated more quantitatively in future work. If reducing the total
570 radiation dose delivered to the cells is an experimental necessity, light sheet-based microscopy
571 approaches offer substantial advantages over confocal microscopy[52]. In our lattice light sheet
572 microscope, a high (30 s) time resolution could possibly be maintained at a lower, more tolerated

573 radiation dose by further decreasing the excitation laser intensities at the sample and acquiring
574 images at even lower SBRs.

575 While *BCM3D 2.0* is capable of segmenting biofilm datasets of lower SBR than previous
576 methods, further modifications to the image processing pipeline may be needed to enable the
577 tracking of extremely light sensitive or highly motile bacterial species. Additional modifications
578 could be made to further improve segmentation accuracy for datasets with even lower SBRs than
579 those successfully segmented here. On the other hand, more sophisticated tracking algorithms
580 could be employed that consider additional features beyond the Euclidian distances between
581 objects. Recently developed deep learning-based cell trackers for both 2D and 3D data[60, 61] are
582 primarily designed for mammalian cells that have very unique cell shapes that can be used to define
583 similarity features that inform cell linking across different frames. To what extent such approaches
584 would improve tracking of bacterial cells that have very homogeneous cell shapes remains to be
585 explored. Further benefits may also be gained by utilizing punctate cell labeling schemes[62] or
586 adaptive microscopy approaches, in which higher illumination intensity frames are interspersed
587 with lower illumination intensity frames and the segmentation results in lower SBR frames are
588 informed by the more accurate results obtained in the higher SBR frames.

589 In summary, the ability to accurately identify and track individual cells in dense 3D
590 biofilms over long periods of time will require the combination of non-invasive and perhaps
591 adaptive fluorescence microscopy approaches for long-term time-lapse imaging, as well as
592 sophisticated image analysis and multi-object tracking tools that provide robust results even for
593 datasets with limited spatial and temporal resolution, and SBR. Here, we have presented an image
594 processing pipeline that enables improved segmentation of dense biofilm-dwelling cells based on
595 3D fluorescence images of low SBR. The feasibility of simultaneous, automated multi-cell

tracking using a simple nearest neighbor tracking algorithm was shown to be feasible if a sufficiently high time resolution can be maintained. The tools developed here can thus be leveraged to improve our understanding of how coordinated behaviors among biofilm-dwelling cells eventually produce in the macroscopic properties of bacterial biofilms.

Acknowledgements

This work was supported in part by the US National Institute of General Medical Sciences Grant 1R01GM139002 (A.G.).

608 **References**

609 1. Nadell, C. D.; Drescher, K.; Foster, K. R., Spatial structure, cooperation and competition
610 in biofilms. *Nature Reviews Microbiology* **2016,** *14* (9), 589.

611 2. Flemming, H. C.; Wingender, J.; Szewzyk, U.; Steinberg, P.; Rice, S. A.; Kjelleberg, S.,
612 Biofilms: an emergent form of bacterial life. *Nat Rev Microbiol* **2016,** *14* (9), 563-75.

613 3. Jayathilake, P. G.; Gupta, P.; Li, B.; Madsen, C.; Oyebamiji, O.; Gonzalez-Cabaleiro,
614 R.; Rushton, S.; Bridgens, B.; Swailes, D.; Allen, B.; McGough, A. S.; Zuliani, P.; Ofiteru, I.
615 D.; Wilkinson, D.; Chen, J.; Curtis, T., A mechanistic Individual-based Model of microbial
616 communities. *PLoS One* **2017,** *12* (8), e0181965.

617 4. Persat, A.; Nadell, C. D.; Kim, M. K.; Ingremeau, F.; Siryaporn, A.; Drescher, K.;
618 Wingreen, N. S.; Bassler, B. L.; Gitai, Z.; Stone, H. A., The mechanical world of bacteria. *Cell*
619 **2015,** *161* (5), 988-997.

620 5. De la Fuente-Núñez, C.; Reffuveille, F.; Fernández, L.; Hancock, R. E., Bacterial biofilm
621 development as a multicellular adaptation: antibiotic resistance and new therapeutic strategies.
622 *Current opinion in microbiology* **2013,** *16* (5), 580-589.

623 6. Frost, I.; Smith, W. P.; Mitri, S.; San Millan, A.; Davit, Y.; Osborne, J. M.; Pitt-Francis,
624 J. M.; MacLean, R. C.; Foster, K. R., Cooperation, competition and antibiotic resistance in
625 bacterial colonies. *The ISME journal* **2018,** *12* (6), 1582-1593.

626 7. Yan, J.; Bassler, B. L., Surviving as a community: antibiotic tolerance and persistence in
627 bacterial biofilms. *Cell host & microbe* **2019,** *26* (1), 15-21.

628 8. Stelzer, E. H., Light-sheet fluorescence microscopy for quantitative biology. *Nature*
629 *methods* **2015,** *12* (1), 23-26.

630 9. Power, R. M.; Huisken, J., A guide to light-sheet fluorescence microscopy for multiscale
631 imaging. *Nature methods* **2017,** *14* (4), 360-373.
632 10. Voleti, V.; Patel, K. B.; Li, W.; Campos, C. P.; Bharadwaj, S.; Yu, H.; Ford, C.; Casper,
633 M. J.; Yan, R. W.; Liang, W., Real-time volumetric microscopy of in vivo dynamics and large-
634 scale samples with SCAPE 2.0. *Nature methods* **2019,** *16* (10), 1054-1062.
635 11. Mimori-Kiyosue, Y., Imaging mitotic processes in three dimensions with lattice light-sheet
636 microscopy. *Chromosome Research* **2021**, 1-14.
637 12. Rosenberg, J.; Cao, G.; Borja-Prieto, F.; Huang, J., Lattice light-sheet microscopy multi-
638 dimensional analyses (LaMDA) of T-cell receptor dynamics predict T-cell signaling states. *Cell*
639 *systems* **2020,** *10* (5), 433-444. e5.
640 13. Manley, H. R.; Potter, D. L.; Heddleston, J. M.; Chew, T. L.; Keightley, M. C.; Lieschke,
641 G. J., Frontline Science: Dynamic cellular and subcellular features of migrating leukocytes
642 revealed by in vivo lattice lightsheet microscopy. *Journal of leukocyte biology* **2020,** *108* (2), 455-
643 468.
644 14. Yordanov, S.; Neuhaus, K.; Hartmann, R.; Díaz-Pascual, F.; Vidakovic, L.; Singh, P.
645 K.; Drescher, K., Single-objective high-resolution confocal light sheet fluorescence microscopy
646 for standard biological sample geometries. *Biomedical optics express* **2021,** *12* (6), 3372-3391.
647 15. Qin, B.; Fei, C.; Bridges, A. A.; Mashruwala, A. A.; Stone, H. A.; Wingreen, N. S.;
648 Bassler, B. L., Cell position fates and collective fountain flow in bacterial biofilms revealed by
649 light-sheet microscopy. *Science* **2020**, eabb8501.
650 16. Parthasarathy, R., Monitoring microbial communities using light sheet fluorescence
651 microscopy. *Current opinion in microbiology* **2018,** *43*, 31-37.

652 17. Heintzmann, R.; Huser, T., Super-Resolution Structured Illumination Microscopy.
653 *Chemical Reviews* **2017,** *117* (23), 13890-13908.
654 18. Gustafsson, M. G.; Shao, L.; Carlton, P. M.; Wang, C. R.; Golubovskaya, I. N.; Cande,
655 W. Z.; Agard, D. A.; Sedat, J. W., Three-dimensional resolution doubling in wide-field
656 fluorescence microscopy by structured illumination. *Biophysical journal* **2008,** *94* (12), 4957-4970.
657 19. Weigert, M.; Schmidt, U.; Boothe, T.; Müller, A.; Dibrov, A.; Jain, A.; Wilhelm, B.;
658 Schmidt, D.; Broaddus, C.; Culley, S., Content-aware image restoration: pushing the limits of
659 fluorescence microscopy. *Nature methods* **2018,** *15* (12), 1090-1097.
660 20. Chen, J.; Sasaki, H.; Lai, H.; Su, Y.; Liu, J.; Wu, Y.; Zhovmer, A.; Combs, C. A.;
661 Rey-Suarez, I.; Chang, H.-Y., Three-dimensional residual channel attention networks denoise and
662 sharpen fluorescence microscopy image volumes. *Nature Methods* **2021,** *18* (6), 678-687.
663 21. Moen, E.; Bannon, D.; Kudo, T.; Graf, W.; Covert, M.; Van Valen, D., Deep learning
664 for cellular image analysis. *Nat Methods* **2019**.
665 22. Jeckel, H.; Drescher, K., Advances and opportunities in image analysis of bacterial cells
666 and communities. *FEMS Microbiology Reviews* **2020**.
667 23. Zhang, M.; Zhang, J.; Wang, Y.; Wang, J.; Achimovich, A. M.; Acton, S. T.; Gahlmann,
668 A., Non-invasive single-cell morphometry in living bacterial biofilms. *Nature communications*
669 **2020,** *11* (1), 1-13.
670 24. Wang, J.; Batabyal, T.; Zhang, M.; Zhang, J.; Aziz, A.; Gahlmann, A.; Acton, S. T. In
671 *LCuts: linear clustering of bacteria using recursive graph cuts*, 2019 IEEE International
672 Conference on Image Processing (ICIP), IEEE: 2019; pp 1575-1579.
673 25. Stringer, C.; Wang, T.; Michaelos, M.; Pachitariu, M., Cellpose: a generalist algorithm
674 for cellular segmentation. *Nature Methods* **2021,** *18* (1), 100-106.

675 26. Weigert, M.; Schmidt, U.; Haase, R.; Sugawara, K.; Myers, G. In *Star-convex polyhedra*
676 *for 3d object detection and segmentation in microscopy*, Proceedings of the IEEE/CVF Winter
677 Conference on Applications of Computer Vision, 2020; pp 3666-3673.
678 27. Scherr, T.; Löffler, K.; Böhland, M.; Mikut, R., Cell segmentation and tracking using
679 CNN-based distance predictions and a graph-based matching strategy. *Plos One* **2020,** *15* (12),
680 e0243219.
681 28. Meyer, F.; Beucher, S., Morphological segmentation. *Journal of visual communication and*
682 *image representation* **1990,** *1* (1), 21-46.
683 29. Otsu, N., A threshold selection method from gray-level histograms. *IEEE transactions on*
684 *systems, man, and cybernetics* **1979,** *9* (1), 62-66.
685 30. Laasmaa, M.; Vendelin, M.; Peterson, P., Application of regularized Richardson–Lucy
686 algorithm for deconvolution of confocal microscopy images. *Journal of microscopy* **2011,** *243* (2),
687 124-140.
688 31. Valm, A. M.; Cohen, S.; Legant, W. R.; Melunis, J.; Hershberg, U.; Wait, E.; Cohen,
689 A. R.; Davidson, M. W.; Betzig, E.; Lippincott-Schwartz, J., Applying systems-level spectral
690 imaging and analysis to reveal the organelle interactome. *Nature* **2017,** *546* (7656), 162.
691 32. Chen, B.-C.; Legant, W. R.; Wang, K.; Shao, L.; Milkie, D. E.; Davidson, M. W.;
692 Janetopoulos, C.; Wu, X. S.; Hammer, J. A.; Liu, Z., Lattice light-sheet microscopy: imaging
693 molecules to embryos at high spatiotemporal resolution. *Science* **2014,** *346* (6208).
694 33. Thormann, K. M.; Saville, R. M.; Shukla, S.; Pelletier, D. A.; Spormann, A. M., Initial
695 Phases of biofilm formation in Shewanella oneidensis MR-1. *J Bacteriol* **2004,** *186* (23), 8096-
696 104.

697 34. Gao, R.; Asano, S. M.; Upadhyayula, S.; Pisarev, I.; Milkie, D. E.; Liu, T.-L.; Singh,
698 V.; Graves, A.; Huynh, G. H.; Zhao, Y., Cortical column and whole-brain imaging with molecular
699 contrast and nanoscale resolution. *Science* **2019,** *363* (6424), eaau8302.
700 35. Schindelin, J.; Arganda-Carreras, I.; Frise, E.; Kaynig, V.; Longair, M.; Pietzsch, T.;
701 Preibisch, S.; Rueden, C.; Saalfeld, S.; Schmid, B., Fiji: an open-source platform for biological-
702 image analysis. *Nature methods* **2012,** *9* (7), 676-682.
703 36. Pettersen, E. F.; Goddard, T. D.; Huang, C. C.; Meng, E. C.; Couch, G. S.; Croll, T. I.;
704 Morris, J. H.; Ferrin, T. E., UCSF ChimeraX: Structure visualization for researchers, educators,
705 and developers. *Protein Science* **2021,** *30* (1), 70-82.
706 37. Parslow, A.; Cardona, A.; Bryson-Richardson, R. J., Sample drift correction following 4D
707 confocal time-lapse imaging. *Journal of visualized experiments: JoVE* **2014,** (86).
708 38. Rudge, T. J.; Steiner, P. J.; Phillips, A.; Haseloff, J., Computational modeling of synthetic
709 microbial biofilms. *ACS synthetic biology* **2012,** *1* (8), 345-352.
710 39. Reshes, G.; Vanounou, S.; Fishov, I.; Feingold, M., Cell shape dynamics in Escherichia
711 coli. *Biophysical journal* **2008,** *94* (1), 251-264.
712 40. Starruß, J.; Peruani, F.; Jakovljevic, V.; Søgaard-Andersen, L.; Deutsch, A.; Bär, M.,
713 Pattern-formation mechanisms in motility mutants of Myxococcus xanthus. *Interface focus* **2012,**
714 *2* (6), 774-785.
715 41. Venkateswaran, K.; Moser, D. P.; Dollhopf, M. E.; Lies, D. P.; Saffarini, D. A.;
716 MacGregor, B. J.; Ringelberg, D. B.; White, D. C.; Nishijima, M.; Sano, H., Polyphasic
717 taxonomy of the genus Shewanella and description of Shewanella oneidensis sp. nov. *International*
718 *Journal of Systematic and Evolutionary Microbiology* **1999,** *49* (2), 705-724.

42. Yan, T.; Richardson, C. J.; Zhang, M.; Gahlmann, A., Computational correction of spatially variant optical aberrations in 3D single-molecule localization microscopy. *Optics express* **2019,** *27* (9), 12582-12599.

43. Liao, P.-S.; Chen, T.-S.; Chung, P.-C., A fast algorithm for multilevel thresholding. *J. Inf. Sci. Eng.* **2001,** *17* (5), 713-727.

44. Van der Walt, S.; Schönberger, J. L.; Nunez-Iglesias, J.; Boulogne, F.; Warner, J. D.; Yager, N.; Gouillart, E.; Yu, T., scikit-image: image processing in Python. *PeerJ* **2014,** *2*, e453.

45. He, K.; Zhang, X.; Ren, S.; Sun, J. In *Deep residual learning for image recognition*, Proceedings of the IEEE conference on computer vision and pattern recognition, 2016; pp 770-778.

46. Zunair, H.; Rahman, A.; Mohammed, N.; Cohen, J. P. In *Uniformizing techniques to process CT scans with 3D CNNs for tuberculosis prediction*, International Workshop on PRedictive Intelligence In MEdicine, Springer: 2020; pp 156-168.

47. Tinevez, J.; Cao, Y., Simple tracker. *MATLAB Cent File Exc* **2016**.

48. Jaccard, P., The distribution of the flora in the alpine zone. 1. *New phytologist* **1912,** *11* (2), 37-50.

49. Wang, J.; Zhang, M.; Zhang, J.; Wang, Y.; Gahlmann, A.; Acton, S. T., Graph-Theoretic Post-Processing of Segmentation With Application to Dense Biofilms. *IEEE Transactions on Image Processing* **2021,** *30*, 8580-8594.

50. Csurka, G.; Larlus, D.; Perronnin, F.; Meylan, F. In *What is a good evaluation measure for semantic segmentation?*, Bmvc, 2013; p 10.5244.

740 51. Matula, P.; Maska, M.; Sorokin, D. V.; Matula, P.; Ortiz-de-Solorzano, C.; Kozubek,
741 M., Cell Tracking Accuracy Measurement Based on Comparison of Acyclic Oriented Graphs.
742 *PLoS One* **2015,** *10* (12), e0144959.
743 52. Zhang, J.; Zhang, M.; Wang, Y.; Donarski, E.; Gahlmann, A., Optically Accessible
744 Microfluidic Flow Channels for Noninvasive High-Resolution Biofilm Imaging Using Lattice
745 Light Sheet Microscopy. *The Journal of Physical Chemistry B* **2021**.
746 53. Liu, R.; Jia, J. In *Reducing boundary artifacts in image deconvolution*, 2008 15th IEEE
747 International Conference on Image Processing, IEEE: 2008; pp 505-508.
748 54. Starck, J.-L.; Pantin, E.; Murtagh, F., Deconvolution in astronomy: A review. *Publications*
749 *of the Astronomical Society of the Pacific* **2002,** *114* (800), 1051.
750 55. Cutler, K. J.; Stringer, C.; Wiggins, P. A.; Mougous, J. D., Omnipose: a high-precision
751 morphology-independent solution for bacterial cell segmentation. *bioRxiv* **2021**.
752 56. Tinevez, J., SIMPLETRACKER a simple particle tracking algorithm that can deal with
753 gaps. *Jean-Yves Tinevez* **2012**.
754 57. Ulman, V.; Maska, M.; Magnusson, K. E. G.; Ronneberger, O.; Haubold, C.; Harder,
755 N.; Matula, P.; Matula, P.; Svoboda, D.; Radojevic, M.; Smal, I.; Rohr, K.; Jalden, J.; Blau,
756 H. M.; Dzyubachyk, O.; Lelieveldt, B.; Xiao, P.; Li, Y.; Cho, S. Y.; Dufour, A. C.; Olivo-
757 Marin, J. C.; Reyes-Aldasoro, C. C.; Solis-Lemus, J. A.; Bensch, R.; Brox, T.; Stegmaier, J.;
758 Mikut, R.; Wolf, S.; Hamprecht, F. A.; Esteves, T.; Quelhas, P.; Demirel, O.; Malmstrom, L.;
759 Jug, F.; Tomancak, P.; Meijering, E.; Munoz-Barrutia, A.; Kozubek, M.; Ortiz-de-Solorzano,
760 C., An objective comparison of cell-tracking algorithms. *Nat Methods* **2017,** *14* (12), 1141-1152.

761 58. Wen, C.; Miura, T.; Voleti, V.; Yamaguchi, K.; Tsutsumi, M.; Yamamoto, K.; Otomo,
762 K.; Fujie, Y.; Teramoto, T.; Ishihara, T., 3DeeCellTracker, a deep learning-based pipeline for
763 segmenting and tracking cells in 3D time lapse images. *Elife* **2021,** *10*, e59187.
764 59. Zhang, M.; Zhang, J.; Wang, Y.; Wang, J.; Achimovich, A. M.; Acton, S. T.; Gahlmann,
765 A., Non-Invasive Single-Cell Morphometry in Living Bacterial Biofilms, GitHub Repository:
766 BCM3D, DOI:10.5281/zenodo.4088658. 2020.
767 60. Magnusson, K. E.; Jalden, J.; Gilbert, P. M.; Blau, H. M., Global linking of cell tracks
768 using the Viterbi algorithm. *IEEE Trans Med Imaging* **2015,** *34* (4), 911-29.
769 61. Moen, E.; Borba, E.; Miller, G.; Schwartz, M.; Bannon, D.; Koe, N.; Camplisson, I.;
770 Kyme, D.; Pavelchek, C.; Price, T.; Kudo, T.; Pao, E.; Graf, W.; Van Valen, D., Accurate cell
771 tracking and lineage construction in live-cell imaging experiments with deep learning. *bioRxiv*
772 **2019**, 803205.
773 62. Qin, B.; Fei, C.; Bridges, A. A.; Mashruwala, A. A.; Stone, H. A.; Wingreen, N. S.;
774 Bassler, B. L., Cell position fates and collective fountain flow in bacterial biofilms revealed by
775 light-sheet microscopy. *Science* **2020,** *369* (6499), 71-77.
776